Prediction of the Near Burner Region and Measurements of NO$_x$ and Particulate Emissions in Heavy Fuel Oil Spray Flames

A. BARREIROS and M. G. CARVALHO*

Department of Mechanical Engineering, Instituto Superior Técnico, 1096 Lisboa Codex, Portugal

M. COSTA and F. C. LOCKWOOD

Department of Mechanical Engineering, Imperial College of Science, Technology and Medicine, London SW7 2BX, UK

Fuel oil combustion is difficult to model because of the lack of detailed knowledge about the spray. In the present article a mathematical model developed at Instituto Superior Técnico and Imperial College is described. The model is validated against data for a combustor fired by an industrial-type swirl burner, for which the initial conditions of the spray have been characterized. With this advantage it is found that a fair simulation of the subsequent aerodynamics and combustion is achieved. Systematic testing has shown that such model failings as exist are linked to the prediction of the gas phase aerodynamics. Improvements will be hard won with recourse to advanced models of turbulence. Burner designs that reduce NO$_x$ emissions are frequently found to do so at the expense of augmented particulates emissions. New data are reported for the emissions of NO$_x$ and particulates as a function of the burner swirl number. With the aid of the present mathematical model the observed trends may be explained. It is concluded that the preferred burner that minimizes the emissions of both is one that ensures rapid droplet vaporization and long residence times for particulates in the internal recirculation zone of the burner. This is an aerodynamically achievable condition.

INTRODUCTION

The simulation of oil combustion poses many problems and requires reliable models of the complex processes of soot and cenosphere formation and destruction. However, detailed information about the fuel spray, required as a boundary condition for computations, is usually not available. Earlier studies [1] have suffered from a lack of information about the spray and this has limited the possibilities of drawing reliable conclusions about the mathematical model. It can be proposed that calculations should commence within the atomizer itself, but this considerably complicates an already difficult task.

The present study benefits from a rather complete set of combustion data collected for an industrial heavy fuel oil (HFO) that includes spray characterization measurements.

This enables the aerodynamic and combustion performance of the mathematical model to be more specifically assessed. A simple model for soot formation is included as soot strongly affects the heat transfer rates and, through the modified densities, the flow. Cenosphere formation and destruction are, however, not modeled since the ability to predict the combustor flow and heat release, which is of interest here, is not significantly influenced by these phenomena.

Most previous HFO studies have considered either NO$_x$ [2–7] or particulates emissions [8, 9]. Because, in most cases, options for reducing NO$_x$ have an adverse effect on particulates [10], emissions studies should encompass both. This problem is addressed and new data reported that reveal the dependence of the emissions of these pollutants on the burner swirl number. The predictions for corresponding operating conditions are then deployed to assist in the physical interpretation of the data.

The ability to validate mathematical models of reacting two-phase flows is usually compro-

mised by the lack of two-phase velocity data and this is also the case here. The measurement task for large flames is far from easy. By way of compensation, a large number of sensitivity studies were performed for several of the existing data sets in order to isolate sources of predictive discrepancies.

EXPERIMENT

Furnace

The cylindrical combustion chamber has a vertical axis to minimize asymmetry due to natural convection and biased ash particle deposition and it is down-fired to facilitate particulate removal. The cylinder comprises ten water-cooled steel segments, each 0.3 m in height and 0.6 m in internal diameter. The roof section and the upper five segments are lined with a 0.09-m-thick layer of refractory and a 0.05-m-thick ceramic fiber blanket sandwiched between the refractory and the water-cooled jacket.

Figure 1 shows the arrangement of the top end wall of the furnace. The burner consists of a central gun and a secondary air supply in a conventional double-concentric configuration, terminating in a refractory quarl. The burner gun comprises a removable plain-jet airblast atomizer and a support pipe that provides a coaxial supply of fuel and air to the nozzle. The atomizer, mounted at the end of the burner gun, consists of a central fuel port surrounded by six equally spaced air ports arranged tangentially around a mixing chamber (Fig. 1).

The fuel is supplied to the burner using a mono-progressing positive displacement pump coupled to a variable-speed motor that is controlled electronically. A loss-in-weight technique incorporating a weighbridge and a timing device ensures the good maintenance of the desired fuel flow rate controlled by the pump speed. The observed variation in flow is within $\pm 3\%$ over a sampling period of 120 s, and negligible over longer periods. The furnace, fuel feeding system, and measurement techniques are fully described in Ref. 11.

Experimental Program and Data Reliability

An extensive experimental program over the last 3 years has generated a large number of
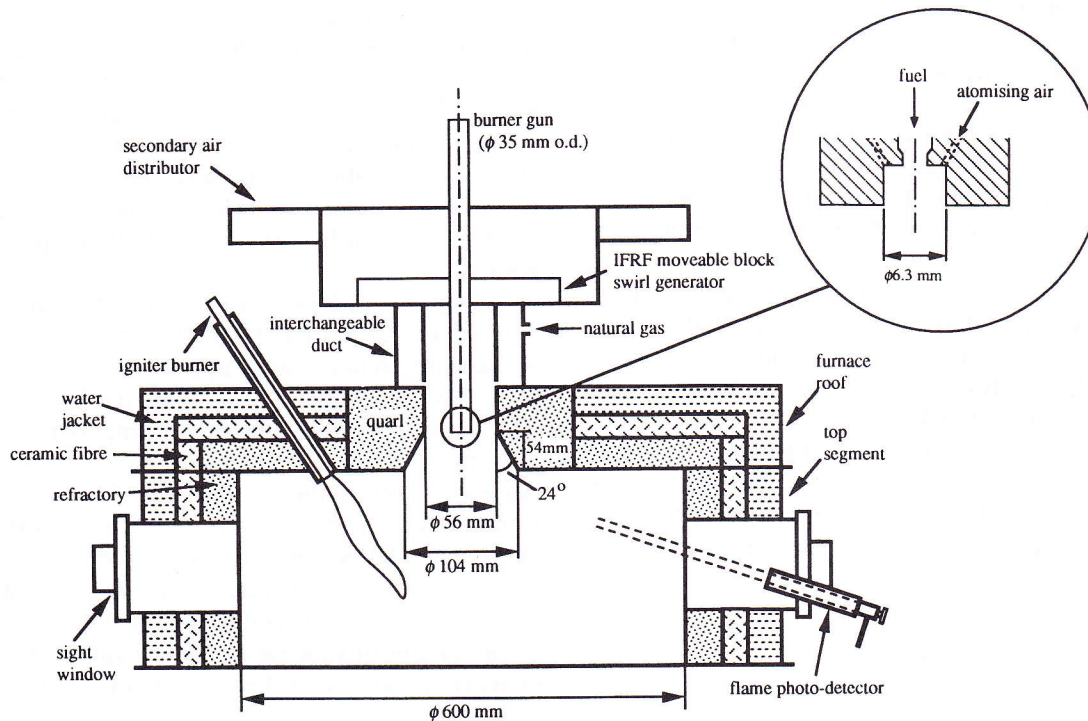
Fig. 1. Furnace roof and burner.

in-flame data for HFO swirl burner flames in the present furnace, details of which are available in [11–13]. The main properties of the HFO used throughout these studies are given in Table 1. The furnace operating conditions for the new emissions data which are reported herein are also given in Table 1. The experiments for a secondary air swirl number (S_s) of 0.9 were arbitrarily selected as the basis for predictive code validation studies which are presented. The comparisons with the other data available [11–13] are entirely analogous to those presented herein.

Prior to the combustion measurements the Malvern 2600 Particle Size Analyzer was used to obtain the droplet size distribution measurements: the Rosin–Rammler function secured a good fit of the data. A 40-μm-diameter platinum/platinum–13% rhodium fine wire thermocouple was used for gas temperature measurements, which led to uncertainties due to radiation losses of about 7% in the regions of highest temperatures and lower elsewhere. A water-cooled, water-quenched probe was used to withdraw the gases for the measurement of the major gas species concentration. Fast quenching of the chemical reactions was achieved and the uncertainty due to the solubility of CO_2 and unburned hydrocarbons in water was negligible.

The measured concentrations of NO$_x$ and particulate emission were obtained with water-cooled stainless-steel probes at the furnace exit ($X/DS = 45$, where X is the axial distance from the burner throat and DS the burner throat diameter: 56 mm), where the gas composition was nearly uniform. For the NO$_x$ measurements, the probe outlet was connected to a heated PTFE line through which the gases were conducted first to a cyclone separator immersed in an ice bath, to eliminate the moisture and the larger particulates from the gas sample, then to a microfiber filter, to remove the remaining particulates, and finally on to a chemiluminescent analyzer. Samples were quenched near the probe tip to about 150°C and condensation of water within the probe was avoided by controlling the inlet temperature of the cooling water (typically to around 60°C). The measured concentrations of NO_2 were typically less than 3% of the total NO$_x$ concentration, and although the NO_2 removed in the cyclone separator by acid formation was negligible, the measured values were nevertheless subject to errors such as that due to the influence of sampling rate on the NO concentration owing to the NO/NO_2 reactions. Only the measured NO$_x$ concentrations are reported. Reproducibility of the data was, on average, within 10%.

TABLE 1

Fuel Characteristics and Furnace Operating Conditions

(a) Characteristics of heavy fuel oil			
Density at 288 K (kg/m^3)	988	Sulfur (wt.%)	2.97
Surface tension at 293 K (N/m)	0.0284	Oxygen (wt. %)	0.44
Dynamic viscosity at 368 K (N · s/m^2)	0.051	Ash (wt.%)	0.04
Carbon (wt.%)	86.4	Asphaltenes (wt.%)	6.9
Hydrogen (wt.%)	9.8	Vanadium (wt. ppm)	53
Nitrogen (wt.%)	0.35	Conradson residue (wt.%)	12.9
Gross calorific value (MJ/kg)	42.5		

(b) Furnace operating conditions			
Fuel mass flow rate (kg/h)	12	Fuel preheat temperature (K)	368
Excess air (%)	15	Atomizing air temperature (K)	293
Secondary air swirl number[a]	0.6–1.3	Secondary air temperature (K)	573
Atomizing air mass flow rate (kg/h)	15	Wall temperature (K)[b]	
Secondary air mass flow rate (kg/h)	170.2	$1 \leq X/DS \leq 11.7$	1423 ± 50
		$11.7 \leq X/DS \leq 22.4$	1323 ± 30

[a] Validation studies performed for $S_s = 0.9$.
[b] For $S_s = 0.9$.

Particulates were collected in a sintered bronze filter, with a maximum pore diameter between 3 and 6 μm placed inside a demountable head of a water-cooled probe (Land Pyrometer Ltd., Sheffield, England). The combustion gases were withdrawn isokinetically through the probe following the procedures recommended in the British Standard BS 893 (1978). On leaving the probe, the moisture was removed by a series of driers and the dry gas flow rate measured using a positive displacement gas meter. The filter was dried in an oven at approximately 110°C to expel any moisture and weighed on a microelectronic balance before and after sampling for each measurement. The quantity of particulates passing through the filter was negligible and radial traverses at the exit sampling location indicated no spatial variation in particulates concentration, with the data reproducible within 10% on average.

Substantial efforts were made to establish and maintain flow symmetry in the furnace [11]. In support of good flow symmetry, radial profiles of the O_2 concentration [12, 13] are reported below for the whole furnace diameter. The repeatability of the data was regularly checked during each experiment. On average all of the data could be reproduced to within 10% of the mean value. The furnace flue-gas was continuously monitored to sense any change in the furnace operating conditions. In addition, although every effort was made to eliminate sources of gas leakage in the furnace construction, the furnace pressure was maintained close to atmospheric. Approximately 55% of the thermal input was transferred through the refractory lining of the five uppermost segments and of the roof section to the enveloping water-cooled jacket. The remaining unlined water-cooled segments were responsible for the extraction of approximately 20% of the thermal input. Heat balance calculations resulted in an unaccountable residual energy of less than 5% of the input.

MATHEMATICAL MODEL

Time-averaged eulerian equations for the conservation of mass, momentum, fuel mixture fraction, enthalpy and soot mass fraction are solved for the gas phase. The standard $k-\varepsilon$ turbulence model [14] is used. The pressure field is calculated from the continuity equation using the PISO algorithm [15]. The calculations are perfomed on a carefully specified finite-difference grid of 54×54 nodes.

A finite number of droplet size ranges are chosen to represent the continuous size distribution of the actual spray. The momentum and thermal balance equations for the droplets are solved in lagrangian fashion. The turbulent dispersion of droplets is simulated using a stochastic separated flow model [16, 17]. The liquid and gas phases are coupled through exchange processes of mass, heat, and momentum, assuming negligible influence of local flow discontinuities induced by the presence of the discontinuous liquid-phase. The droplet-gas coupling is incorporated in the numerical procedure using the PSIC technique [18]. Due to the stochastic nature of the procedure, a large number of droplets have been considered in order to obtain an acceptable representation of the average spray distribution inside the furnace.

In the spray combustion model, it is assumed that the droplets act as distributed sources of fuel which evaporate to form a cloud of vapor (see Appendix). The fuel vapor diffuses to the flame front, where it burns instantaneously and irreversibly and in an one-step reaction with the oxidant. The effects of the turbulent fluctuations of mean species concentrations, density, and temperature are simulated by adopting a statistical approach that assumes that the mixture fraction fluctuations are described by a clipped gaussian probability density function [19].

The problematical matter of simulating the formation of and destruction of soot must, to a limited extent, be addressed when modeling HFO flames. Very little of the fuel carbon appears as soot so the primary function of the soot model is the good characterization of the optical properties of the flame. The soot contents and sizes of typical HFO flames are generally so large that the blackbody limits are approached and, as a consequence, the accurate prediction of soot is not a prerequisite for the good calculation of the radiation heat transfer. To simulate the soot production a

simple global expression is used [20]:

$$S_f = C_f P_f \phi^n \exp\left(-\frac{E}{RT_g}\right),\qquad(1)$$

where P_f, ϕ, R, and T_g are the fuel partial pressure, the equivalent ratio, the universal gas constant and the local gas temperature. The soot formation constant C_f is taken as 0.01 kg/(N · m · s) from Ref. 1 and n as 3 and the activation energy for soot formation E as 168 kJ/mol are taken from Ref. 20. Following Ref. 20 the lower and upper soot flammability limits have been set to 2 and 8. Since soot is produced in the immediate vicinity of the droplets the calculation of soot is based on the near droplet mixture fraction [1]: $\bar{f}_d = (1 + \bar{f})/2$, where $\bar{f}$ is the calculated mean mixture fraction. A simple method for estimating the rate of soot burning is used [21]. Following conventional turbulence concepts, the model presumes that turbulence decay of the mixing rate is proportional to the magnitude of the time mean soot concentration m_s, and to the time-scale of the large-scale turbulence motion ε/k. Depending on the oxygen concentration the overall soot burning rate is given by

$$S_d = Am_s\frac{\varepsilon}{k}\min\left(1,\frac{m_{ox}}{m_s s_s + m_f s_f}\right),\qquad(2)$$

where A is a model constant assigned the value 4 [21], m_{ox} and m_f are the local mean concentrations of oxygen and fuel, and s_s and s_f are the stoichiometric oxygen requirement of soot and fuel.

An accurate treatment of the thermal radiation transfer is essential to the proper prediction of HFO combustion. The present model is based on the method of Ref. 22, where the fundamental radiation transfer equation is solved within discretized solid angles, here suitably modified for the axisymetric geometry. At each elemental solid angle the radiant intensity of a pencil of rays is assumed to be concentrated along a particular ray. The change in intensity of a ray traveling in a specified direction through an absorbing and emitting medium at temperature T_g is described by

$$\frac{dI}{ds} = -kI + k\frac{\sigma T_g^4}{\pi},\qquad(3)$$

where k is the absorption coefficient and σ is the Stefan–Boltzman constant. Equation 3 is analytically integrated to yield the following recurrence relation:

$$I_{n+1} = \frac{\sigma T_g^4}{\pi}(1 - \exp(-ks)) + I_n \exp(-ks),\qquad(4)$$

where I_n and I_{n+1} are the intensities of the ray on entry to and exit from a control volume and s is the distance traveled. From Eq. 4 a radiation source term for the energy equation is obtained:

$$S_n = (I_n - I_{n+1})\Omega d\Omega dA,\qquad(5)$$

where dA is the area covered by the solid angle $d\Omega$ with the direction of Ω. Considering the representative directions defined by discretizing the hemisphere centered on specified wall grid points, Eq. 4 is applied successively when a ray is traced between two opposite wall points, until the arriving intensity at each wall grid point is known.

To calculate the gaseous absorption coefficient the two-grey-plus-clear-gas model [23] is used. The optical behavior of the soot is accommodated, again following [23], by discretizing the soot absorption coefficient such that it is uniform at empirically determined values within each of the bands of the grew-plus-clear-gas model.

RESULTS AND DISCUSSION

Prediction of the Near Burner Region

The initial conditions for the spray calculations were based on the experimental data obtained under nonreacting conditions [11–13]. The measured droplet size distribution averaged over the width of the spray 75 mm downstream[1] of the atomizer exit plane (Rosin–Rammler parameters: $\bar{X} = 53\ \mu$m, $N = 1.5$)

---

[1] Measurements closer to the atomizer were not obtainable owing to high obscuration [11].

was discretized into 15 size ranges. Photographic evidence [11] showed that the liquid breakup process was completed close to the atomizer exit. It may be presumed that the amount of droplet vaporization was negligible between breakup and measurement. Computations were, therefore, initiated at the atomizer exit for the experimental size distribution with the droplets emanating from ten starting locations uniformly distributed over the inlet plane. For each size range and starting location, random trajectories for a sample of 20 droplets were tracked. Initial droplet velocities were estimated based on high-speed photographs of the nonreacting sprays [11]; values of between 20 and 40 m/s were obtained. Finally, a parabolic inlet fuel mass distribution was assumed based on measurements obtained with a radial patternator [11].

In the absence of two-phase velocity measurements, Fig. 2 (see insert at beginning of this article) shows the predicted gas flow pattern and droplets' trajectories in the near burner region (NBR) together with a photograph of the flame. The apparent similarity of the principal flow features is reassuring. The value of S_s used (0.9) is large enough to generate a strong internal recirculation zone (IRZ). An external recirculation zone (ERZ) is established due to flow separation at the quarl exit. The IRZ plays the crucial role in the stabilization process of the present flame. This is a result of the primary jet, containing the droplets, being directly introduced into the IRZ, which it penetrates to an extent dependent upon its momentum and the degree of combustion air swirl. The fast mixing of droplets with the hot recirculated gases in the IRZ results in high vaporization rates.

Figure 3 shows the comparisons between predicted and measured radial profiles of oxygen and gas temperature at several axial stations. At $X/\mathrm{DS} = 1.14$, reliable gas temperature measurements could not be obtained owing to the impingement of an excess of droplets on the thermocouple wires. On the whole the agreement is satisfactory, except at $X/\mathrm{DS} = 2.21$, where significant discrepancies occur. Many remedies have been tried, all without success. Apart from grid refinement experiments, these included: fairly drastic changes in the spray initial conditions (e.g., droplet size
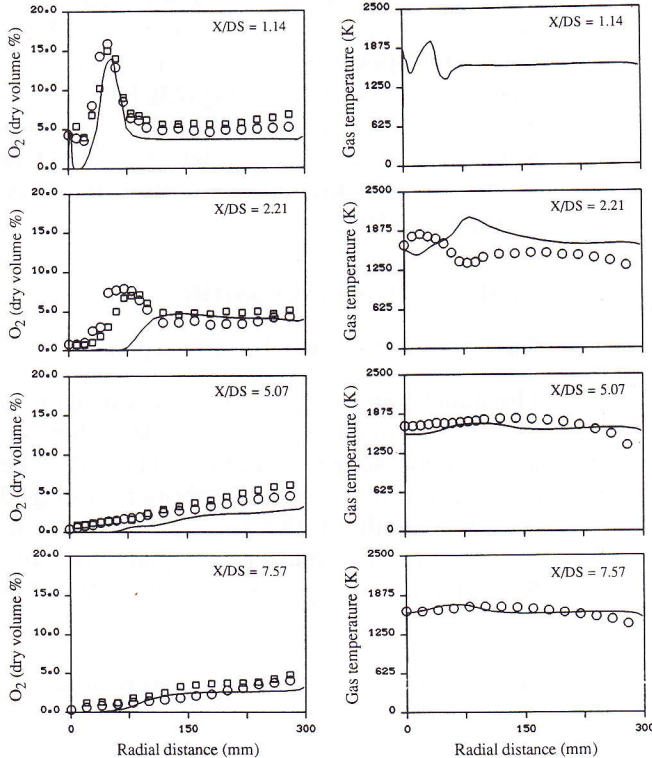
Fig. 3. Measured and predicted oxygen concentrations and gas temperatures (experimental: ○ near probing side, □ far probing side; prediction: —).

distribution and droplet velocities as well as fuel mass distribution) and initial gas velocity profiles and turbulence levels.

The discrepancies at $X/DS = 2.21$, are further explored in Fig. 4(a), which shows the predicted and measured oxygen concentrations, together with the calculated contours of zero axial velocity and the (normalized) stream functions that define the boundaries of the IRZ and ERZ. It may be observed that at $X/DS = 2.21$ the experimental oxygen concentration peak ($r \approx 75$ mm), an indicator of the presence of the secondary air flow around the "real" IRZ, is well inside of the predicted IRZ. The quality of the predicted oxygen concentration profiles could be suitably adjusted by decreasing S_s to 0.5 as shown in Fig. 4b, but such a "fix" has no justification. It serves only to demonstrate the dependency of the intricacies of the NBR flow on the burner aerodynamics.

Measurements of NO$_x$ and Particulate Emissions

Figure 5 shows the concentrations of NO$_x$ and particulates in the flue-gas as a function of S_s.

Both NO$_x$ and particulate emissions significantly decrease on increasing S_s from 0.6 up to about 0.9, beyond which a further increase in S_s up to 1.3 causes only small, but opposing, variations: the NO$_x$ continues to decrease while the particulates increase.

Emissions of NO$_x$, for HFO combustion, have two sources: nitrogen in the combustion air ("prompt" and "thermal" NO$_x$) and nitrogen compounds in the fuel ("fuel" NO$_x$). There is a general agreement that as a first approximation "prompt" NO$_x$ can generally be neglected [10]. On the other hand, there is some experimental evidence [4, 5] to suggest that "fuel" NO$_x$ is the dominant contributor to total NO$_x$ emissions. For example, even with a relatively small amount of fuel nitrogen (0.24 wt.%), "fuel" NO$_x$ formation was shown to be responsible for about 50% of the total NO$_x$, with fuels of higher nitrogen content showing a relatively greater contribution of "fuel" NO$_x$ [5]. Against this background and the knowledge of the computed flow patterns Fig. 5 may be interpreted as follows: at low values of S_s the jet crosses the fuel-rich IRZ so that "fuel" NO$_x$ (and "prompt" NO$_x$) formation is encour-

(a)   (b)
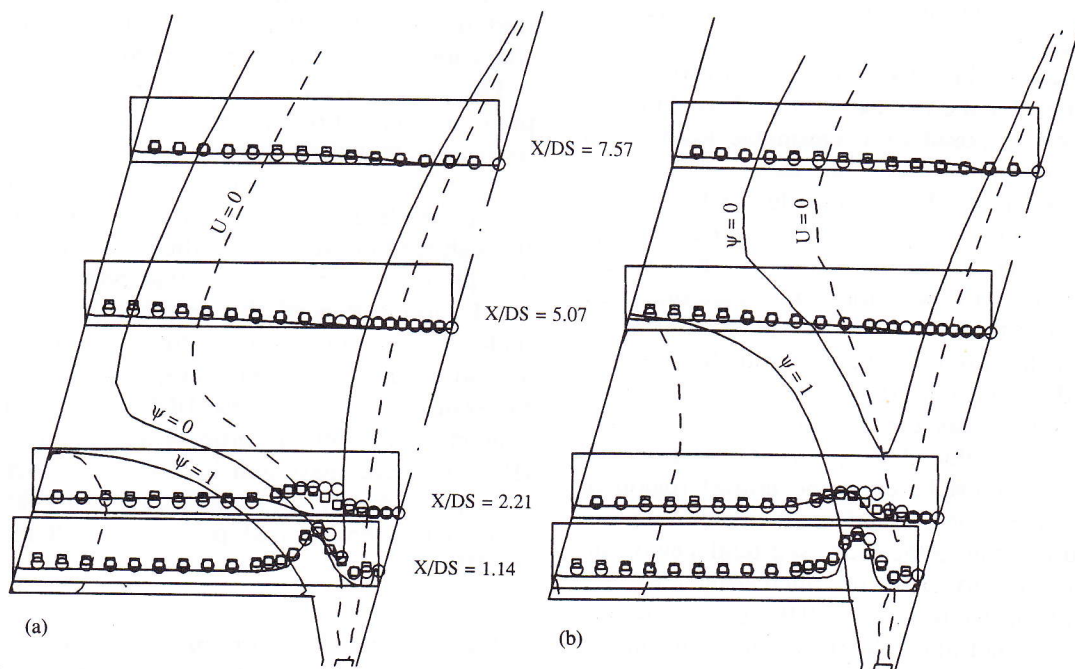
Fig. 4. Composite of measured and predicted oxygen concentrations (experimental oxygen: ○ near probing side, □ far probing side; predicted oxygen: —) and predicted contours of zero axial velocity and streamlines ($\psi = 0$ and $\psi = 1$) which define boundaries of the IRZ and ERZ. (a) Experimental data and predictions for $S_s = 0.9$. (b) Experimental data for $S_s = 0.9$ and predictions for $S_s = 0.5$.
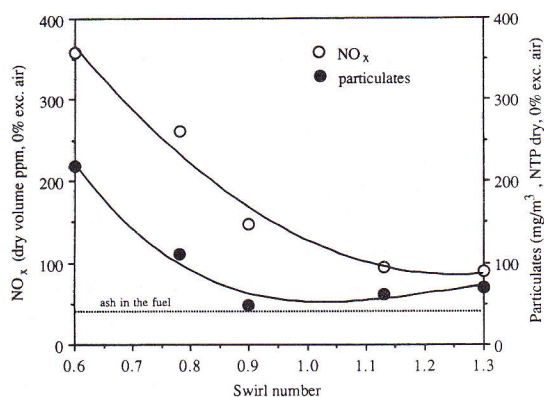
Fig. 5. Influence of S_s on measured NO_x and particulate emissions. Dotted line represents value for emissions assuming 100% conversion of carbon.

aged owing to partial droplet vaporization in regions with relatively high O_2 concentrations. Increasing S_s strengthens the IRZ, thereby increasingly confining droplet vaporization within the fuel-rich IRZ. This results in progressively less fuel-N conversion to NO_x (and less "prompt" NO_x). The increase in "thermal" NO_x formation with increasing S_s due to the higher NBR gas temperatures [13] eventually serves to attenuate the decrease in the total NO_x emissions for values of S_s in excess of about 0.9.

Since the initial droplet size distribution is constant for the five experimental conditions it may be supposed with reasonable justification [24] that similar cenospheres are formed regardless of S_s. The time-scale for the formation of the cenospheres may be expected to shorten as S_s increases due to increasingly rapid droplet vaporization and, therefore, their residence times in the NBR will be determined by the locality of formation and the penetration depth into the IRZ. The lowest particulate emission occurs for $S_s \approx 0.9$, suggesting that this is the value that optimizes the residence times of cenospheres in the hottest region of the flame. For $S_s < 0.9$, particulates increase rapidly owing to the increased tendency of the central jet to cross the increasingly weaker IRZ. Conversely for $S_s > 0.9$ a gradual reduction in penetration depths of the cenospheres into the increasingly stronger IRZ can be anticipated; this reduces their residence times there and leads to a higher proportion of ceno-

spheres leaving the crucial IRZ and, hence, higher particulate emissions as the value of S_s approaches 1.3.

The overall performance of the present combustor is typical of a good industrial one; specifically, and referring to Fig. 5, the unburned carbon as a percentage of that in the original fuel varies between 0.2% for $S_s = 0.6$ and 0.01% for $S_s = 0.9$.

CONCLUDING REMARKS

The ability to predict the combustion/ aerodynamics of fuel oil flames is compromised by the need for information about the velocities and size distribution of the droplets emanating from the burner gun. When this information is reasonably complete, as in the present work, the complexities of the two-phase flow in the NBR can be simulated to a useful degree. Nonetheless, predictive deficiencies are all too evident.

In the present study, and in the absence of much needed reliable two-phase velocity data, it is concluded that the failings are linked to the aerodynamic forecasts. The flow field near an industry-type oil swirl burner is characterized by subtleties that exceed those of the conventional $k-\varepsilon$ turbulence model.

The physical insight which the present computations has afforded leads to the central conclusion that the recurring conflict between a burner with low NO_x emissions and one with low particulates emissions may be resolved through careful attention to the aerodynamics. The preferred burner is one that provides (a) rapid vaporization of the droplets to ensure fuel-rich conditions during this phenomenon and so reduced NO_x emissions, promoted by, for example, a fairly intense IRZ, and (b) long residence times of the primary stream in the IRZ to ensure maximum burnout of particulates, promoted by, for example, a primary flow of high momentum that penetrates well into the IRZ.

APPENDIX

A two-stage droplet life history was assumed: heat up to the boiling temperature with no evaporation followed by heat transfer controlled vaporization. The rate of change of droplet temperature is computed from

$$\frac{dT_d}{dt} = \frac{6k_g \text{Nu}}{\rho_d Cp_d D_d^2}(T_g - T_d), \tag{A1}$$

where k_g is the gas thermal conductivity, ρ_d and Cp_d are the density and specific heat of the droplet, and the Nusselt number is given by [1]:

$$\text{Nu} = 2.0 + 0.55 Re_d^{1/2} Pr^{1/3} \tag{A2}$$

Re$_d$ is the droplet Reynolds number defined as

$$\text{Re}_d = \frac{\rho_g D_d |\vec{V}_g - \vec{V}_d|}{\mu_g}. \tag{A3}$$

The rate of droplet diameter diminution is given by

$$\frac{dD_d}{dt} = -C \frac{4k_g}{\rho_d Cp_g D_d} \ln(1 + B), \tag{A4}$$

where B is the transfer number:

$$B = \frac{Cp_g(T_g - T_d)}{L}, \tag{A5}$$

where L is the latent heat of vaporization, and C is an empirical correction factor to account for the effect of convection on the evaporation rate [25]:

$$C = 1 + \frac{0.278(Re_d^{1/2} Pr^{1/3})}{\left(1 + \dfrac{1.237}{Re_d Pr^{4/3}}\right)^{1/2}}. \tag{A6}$$

The equations above are analytically integrated to yield the following recurrence equations:

$$T_{d,i+1} = T_g + (T_{d,i} - T_g)\exp\left(-\frac{6k_g \text{Nu}}{\rho_d Cp_d D_d^2}\Delta t\right), \tag{A7}$$

$$D_{d,i+1} = \left(D_{d,i}^2 - C\frac{8k_g \ln(1+B)}{\rho_d Cp_d}\Delta t\right)^{1/2}. \tag{A8}$$

REFERENCES

1. Abbas, A. S., and Lockwood, F. C., *ASME J. Eng. Gas Turbines Power* 107:726 (1985).
2. Turner, D. W., Andrews, R. L., and Siegmund, C. W., *AIChE Symp. Ser.* 68:55 (1972).
3. Pershing, D. W., Martin, G. B. and Berkau, E. E., *AIChE Symp. Ser.* 71:19 (1975).
4. Pershing, D. W., Cichanowicz, J. E., England, G. C., Heap, M. P., and Martin G. B., *Seventeenth Symposium (International) on Combustion*, The Combustion Institute, Pittsburgh, 1979, p. 715.
5. Pershing, D. W., England, G. C., Heap, M. P., and Flament, G., *AIChE Symp. Ser.* 76:1 (1980).
6. Beér, J. M., Jacques, M. T., Farmayan, W., and Taylor, B. R., *Eighteenth Symposium (International) on Combustion*, The Combustion Institute, Pittsburgh, 1981, p. 101.
7. England, G. C., Heap, M. P., Pershing, D. W., Nihart, R. K., and Martin, G. B., *Eighteenth Symposium (International) on Combustion*, The Combustion Institute, Pittsburgh, 1981, p. 163.
8. Goldstein, H. L., and Siegmund, C. W., *Environ. Sci. Technol.* 10:1109 (1976).
9. Whitehead, D. M., Finn, J. C., and Beadle, P. C., *Erdöl and Kohle*, Erdgas, Petrochemie/Hydrocarbon Technology 36:577 (1983).
10. Kelly, F. T., Liddy, J. P., Sutherland, H., Sutton, G. W., and Whitehead, D. M., *Erdöl und Kohle*, Erdgas, Petrochemie/Hydrocarbon Technology 42:408 (1989).
11. Costa, M., Ph.D. thesis, University of London, 1992.
12. Costa, M., Costen, P., and Lockwood, F. C., *Combust. Sci. Technol.* 75:129 (1991).
13. Costa, M., Costen, P., and Lockwood, F. C., *Combust. Sci. Technol.* 77:1 (1991).
14. Launder, B. E. and Spalding D. B., *Mathematical Models of Turbulence*, Academic, New York, 1972.
15. Issa, R. I., *J. Comp. Phys.* 62:40 (1986).
16. Dukowicz, J. K., *J. Comp. Phys.* 35:229 (1980).

17. Gosman, A. D., and Ioannides, E., AIAA paper no. 81-0323 (1981).

18. Crowe, C. T., Sharma, C. P., and Stock, D. E., *ASME J. Fluids Eng*. 99:325 (1977).

19. Lockwood, F. C., and Naguib, A. S., *Combust. Flame* 24:109 (1975).

20. Khan, I. M. and Greeves, G., *Heat Transfer in Flames* (Afgan and Beér, Eds.), Hemisphere, New York, 1974, p. 391.

21. Magnussen, B. F., and Hiertager, B. H., *Sixteenth Symposium (International) on Combustion*, The Combustion Institute, Pittsburgh, 1976, p. 719.

22. Lockwood, F. C., and Shah, N. G., *Eighteenth Symposium (International) on Combustion*, The Combustion Institute, Pittsburgh, 1981, p. 1405.

23. Truelove, J. S., AERE Harwell Report no. HL 76/3448/KE (1976).

24. Urban, D. L., and Dryer, F. L., *Twenty-Third Symposium (International) on Combustion*, The combustion Institute, Pittsburgh, 1991, p. 1437.

25. Faeth, G. M., and Lazar, R. S., *AIAA J*. 9:2165 (1971).
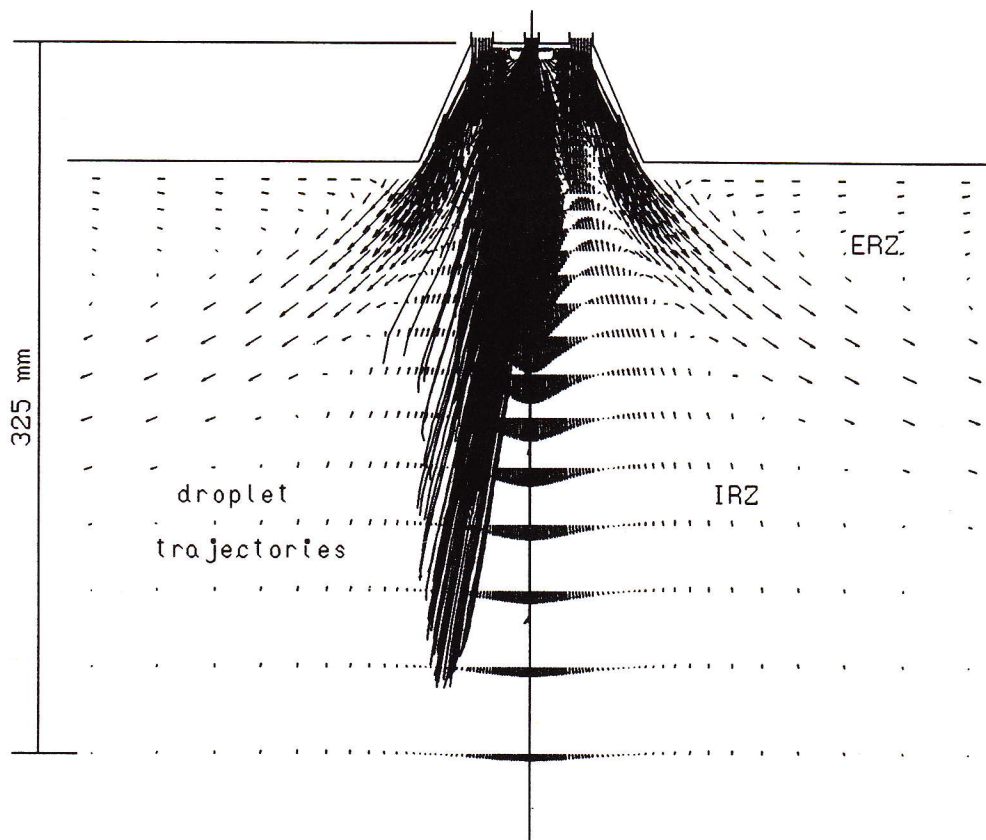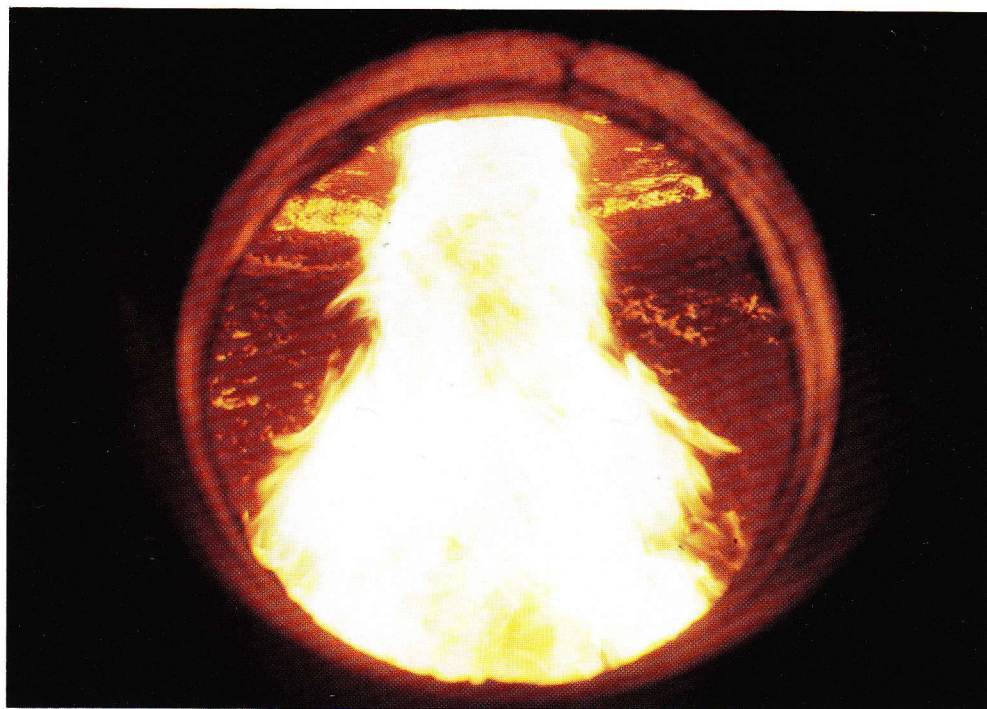
Fig. 2. Composite of predicted gas flow pattern, droplet trajectories and flame photograph.